ARTICLE

Metastability of Palladium Carbide Nanoparticles during Hydrogen Release from Liquid Organic Hydrogen Carriers

Received 00th January 20xx,
Accepted 00th January 20xx

DOI: 10.1039/x0xx00000x

Ralf Schuster,[a] Manon Bertram,[a] Henning Runge,[b] Simon Geile,[b] Simon Chung,[b] Vedran Vonk,[b] Heshmat Noei,[b] Agnieszka Poulain,[c] Yaroslava Lykhach,*[,a] Andreas Stierle,[b,d] and Jörg Libuda*[,a]

Efficient hydrogen release from liquid organic hydrogen carriers (LOHCs) requires a high level of control over the catalytic properties of supported noble metal nanoparticles. Here, the formation of carbon-containing phases under operation conditions has a direct influence on the activity and selectivity of the catalyst. We studied the formation and stability of carbide phases using well-defined Pd/α-Al_2O_3(0001) model catalysts during dehydrogenation of a model LOHC, methylcyclohexane, in a flow reactor by in-situ high-energy grazing incidence X-ray diffraction. The phase composition of supported Pd nanoparticles was investigated as a function of particle size and reaction conditions. Under operating conditions, we detected the formation of a Pd_xC phase followed by its conversion to Pd_6C. The dynamic stability of the Pd_6C phase results from the balance between uptake and release of carbon by the supported Pd nanoparticles in combination with the thermodynamically favorable growth of carbon deposits in the form of graphene. For small Pd nanoparticles (6 nm), the Pd_6C phase is dynamically stable under low flow rate of reactants. At the high reactant flow, the Pd_6C phase decomposes shortly after its formation due to the growth of graphene. Structural analysis of larger Pd nanoparticles (15 nm) reveals the formation and simultaneous presence of two types of carbides, Pd_xC and Pd_6C. Formation and decomposition of Pd_6C proceeds via a Pd_xC phase. After an incubation period, growth of graphene triggers the decomposition of carbides. The process is accompanied by segregation of carbon from the bulk of the nanoparticles to the graphene phase. Notably, nucleation of graphene is more favorable on bigger Pd nanoparticles. Our studies demonstrate that metastability of palladium carbides associated with dynamic formation and decomposition of the Pd_6C and Pd_xC phases is an intrinsic phenomenon in LOHC dehydrogenation on Pd-based catalysts and strongly depends on particle size and reaction conditions.

1. Introduction

Liquid organic hydrogen carriers (LOHCs) enable storage of energy obtained from intermittent renewable sources such as wind and solar power.[1-3] The LOHC technology involves reversible hydrogenation and dehydrogenation of heterocyclic organic compounds which are liquid in pure form or in the form of mixtures.[2-4] Typically, N-ethylcarbazole, indole, methylcyclohexane, or dibenzyltoluenes store about 5-8 wt% hydrogen at ambient conditions.[5-6] The stored hydrogen is released by dehydrogenation of the LOHC over a noble metal catalyst at elevated temperatures. The latest research progress in the LOHC technology and development of the LOHC catalysts has been summarized in recent reviews (see e.g. refs. 7-10).

Previously, the detailed mechanism of LOHC dehydrogenation was investigated using model catalysts such as well-ordered Pt(111) and Pd(111) single crystals[6, 11-14] and well-defined Pt and Pd supported nanoparticles.[15-17] It was found that dehydrogenation of both homocyclic and N-heterocyclic LOHCs involves multiply dehydrogenated intermediates. The complete unloading of LOHCs is challenging because of kinetic and thermodynamic limitations and, to some extent, may also yield carbonaceous byproducts.[6, 11] For instance, dehydrogenation of methylcyclohexane on Pt(111) involves π-allylic species which dehydrogenate to a phenyl ring. However, this step is accompanied by a C–H bond scission in methyl group resulting in benzyl.[13] This undesired reaction impedes the desorption of fully unloaded counterpart of methylcyclohexane, toluene. Generally, further dehydrogenation of phenyl rings and C–H bond scission in methyl/methylene functional groups upon unloading of related LOHCs (e.g. dicyclohexylmethane) yields similar decomposition fragments which are the main source of the surface carbon above 450 K on both Pt(111) and Pd(111).[11] With respect to the dehydrogenation efficiency, palladium is among the most efficient catalysts for LOHC dehydrogenation. It was suggested that the presence of co-adsorbates and their diffusion into the subsurface have a direct influence on the mechanism of LOHC dehydrogenation over Pd catalyst.[11] Diffusion of hydrogen and carbon into the bulk of Pd is well

[a] Interface Research and Catalysis, ECRC, Friedrich-Alexander-Universität Erlangen-Nürnberg, Egerlandstraße 3, 91058 Erlangen, Germany.
[b] Deutsches Elektronen-Synchrotron DESY, Notkestrasse 85, 22607 Hamburg, Germany.
[c] European Synchrotron Radiation Facility, 71 Avenue des Martyrs, 38000 Grenoble, France.
[d] Fachbereich Physik, Universität Hamburg, Jungiusstrasse 11, 20355 Hamburg, Germany.

†Electronic Supplementary Information (ESI) available: [XRR, particle size distribution based on SEM, analysis of overlapping intensities of the Bragg reflection and Debye-Scherrer ring in 2D reciprocal space maps obtained from 15 nm Pd/α-Al_2O_3(0001) model catalyst]. See DOI: 10.1039/x0xx00000x

documented in literature and the influence of the corresponding hydride and carbide phases on the activity and selectivity of the catalyst has been widely discussed.[18-22]

Under the conditions of LOHC dehydrogenation, hydrogen diffusion into the Pd bulk is suppressed by the low stability of β-hydride phases above 500 K.[24] However, the formation of surface carbon and its diffusion into the bulk in this temperature range is of particular interest.[25-27] In the limit of low carbon concentration, diffusion into the bulk is thermodynamically favorable.[28-32] In particular, it has been shown that subsurface diffusion is facile on stepped surfaces and on nanoparticles.[33-34] At higher carbon concentration, however, density functional theory (DFT) predicts a competition between the diffusion into the subsurface region and the formation of carbon clusters on the surface.[34-35] In the bulk, carbon atoms occupy interstitial octahedral sites, giving rise to an increase of the lattice parameter.[36-38] Typically, two carbide phases are observed, which differ with respect to carbon content, i.e. α–Pd_xC (1-2% C) and β–Pd_xC (11-16% C).[32] Dissolution of carbon leads to formation of α–Pd_xC which is considered the precursor to the β–Pd_xC phase. However, even the most stable palladium carbide phase, Pd_6C, was found to be thermodynamically less favorable with respect to graphite.[29] It was argued that the formation of carbide occurs because the growth of graphene is delayed due to the large critical size of nucleus (about 5 nm as predicted on Pd(100)).[29] At the onset of graphene nucleation, the precursor structures consisting of carbon filaments with a length of a few nanometers were observed on supported Pd nanoparticles.[30-31] It is not clear, however, whether the nucleation of graphene or its precursor structures eventually leads to decomposition of the carbide phase. Based on DFT calculations, the graphene adsorption on the carbide surface is slightly less energetically favored with respect to the pure Pd(111) surface.[30] Although carbon obtained by the decomposition of hydrocarbons at the surface is considered the main source,[31] alternative mechanisms of graphene growth involving carbon segregation from the bulk were also proposed.[39]

In this work, we investigate the formation of palladium carbide phases using well-defined Pd/α-Al_2O_3(0001) model catalysts. We employ high-energy grazing incidence X-ray diffraction (HE-GIXRD) under the conditions of catalytic LOHC dehydrogenation to monitor the phase composition of supported Pd nanoparticles as a function of particle size and reactant flow rate. HE-GIXRD is a powerful method to study changes of the lattice parameter and the formation of new phases in supported noble metal nanoparticles under operando conditions.[40-47] Using synchrotron radiation, we reach a temporal resolution on the order of 1 s in the in-situ experiment. As a model LOHC, we use methylcyclohexane which has a similar surface chemistry as the heteroatom-free LOHCs that are currently favored in technical applications (mixtures of dibenzyltoluenes[8-9]). Our study shows that the phase composition is highly dynamic under operation conditions. The formation and decomposition of carbon-containing phases are controlled by kinetic and thermodynamic effects and depend strongly on the particle size.

2. Experimental

The high-energy grazing incidence X-ray diffraction (HE-GIXRD) study was performed at Beamline ID31 at the European Synchrotron Radiation Facility (ESRF), Grenoble, France. GIXRD patterns were recorded with an X-ray photon energy of 78 keV using a high-energy 2D detector Pilatus3 X CdTe 2M with a pixel size of 172 microns. The experiments were performed in a flow reactor (Leiden Probe Microscopy) similar to this described in ref. 48. The total pressure and the gas composition in the flow reactor were controlled by means of a mass-flow-controlled gas dosing system.

Well-defined Pd/α-Al_2O_3(0001) model catalysts were prepared in an UHV setup at the DESY NanoLab.[49] Briefly, the α-Al_2O_3(0001) substrates were first degassed at 873 K for two hours. Subsequently, the substrates were exposed to an oxygen cracker (p_{O2} = 1×10^{-7} mbar, T = 748 K) to heal the oxygen vacancies. Finally, Pd metal was deposited in UHV by means of physical vapor deposition (PVD) from an electron beam evaporator at a deposition rate of 3.5×10^{13} atoms×cm^{-2}×s^{-1} (5.0×10^{-3} nm×s^{-1}) and a sample temperature of 873 K. Here, the deposition rate was determined based on the X-ray reflectometry (XRR) analysis and the deposition time (see Supporting Information, Figure S1).

Two Pd/α-Al_2O_3(0001) samples were prepared with apparent average diameters of the supported Pd nanoparticles of 6 and 15 nm as determined by a Scherrer analysis of the full width at half maximum (FWHM) of the Pd(111) Bragg peaks.[50] Here, the apparent mean particle sizes were determined by averaging over all orientations obtained from the radial analysis of the 2D diffraction patterns (vide infra) under assumption of a spherical shape of the Pd nanoparticles. Note, that further line broadening effects like strain were neglected.

The size distribution of the Pd nanoparticles was studied by means of Scanning Electron Microscopy (SEM) (see Supporting Information, Figure S2). The analysis of the SEM images was performed with the software ImageJ. Based on the size distribution histogram, the average diameter of the Pd nanoparticles is 14.2 ± 3.5 nm. This value is in a good agreement with the size of Pd nanoparticles determined by a Scherrer analysis. The corresponding particle density is 2.7×10^{15} m^{-2}.

The samples were transferred into the flow reactor under ambient atmosphere and cleaned in-situ before each experiment by oxidation and reduction cycles. Specifically, the cycles consisted of 10 min exposure to O_2 (10^{-5} mbar) at 670 K followed by a reduction with H_2 (10^{-5} mbar) at 620 K for 30 min. The clean Pd/α-Al_2O_3(0001) samples were then kept under pure Ar flow. Methylcyclohexane (MCH) was introduced into the flow reactor from an independent gas line using Ar as a carrier gas. Based on the vapor pressure, we estimate a partial pressure of MCH of 48 mbar. The total pressure of the reactants in the flow reactor was set to 1000 mbar for each individual experiment with the flow rates set either to 5 ml/min (low flow) or to 100 ml/min (high flow). All experiments were performed at a sample temperature of 500 K.

For detailed analysis, the intensities of the Bragg reflections in the 2D reciprocal space maps were displayed on a logarithmic

scale using a Matlab routine. This procedure magnifies minor diffraction patterns and allows to detect new phases with high accuracy. The logarithmic intensity profiles (Log_{10}Intensities) were obtained from the 2D reciprocal space maps along radial direction and fitted with Voigt profiles.

3. Results and Discussion

3.1. MCH dehydrogenation over small Pd nanoparticles (6 nm) at low gas flow rate

A portion of the 2D reciprocal space map around the Pd(111) Bragg reflection obtained from the 6 nm Pd/α-Al_2O_3(0001) under Ar at a flow rate of 5 ml/min at 500 K is shown in Figure 1a. Analysis of the data was performed by monitoring the intensity profile of the Pd(111) Bragg reflection along the radial direction indicated by the red line in Figure 1a. The evolution of the intensity of the Bragg reflection under the exposure to two consecutive pulses of MCH at 500 K is plotted in Figure 1b as a function of time and diffraction angle 2Θ.

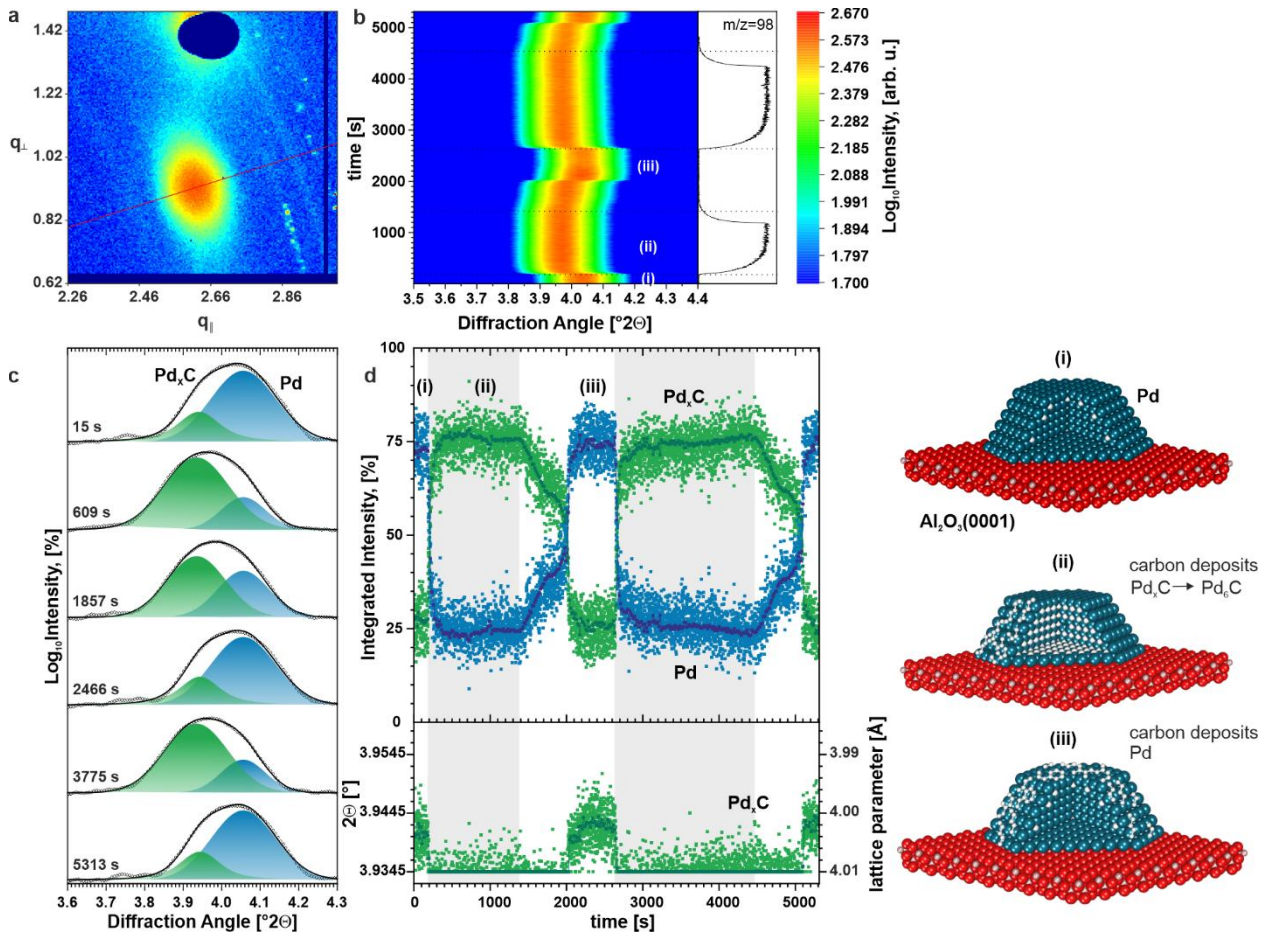

Figure 1. Small Pd nanoparticles (diameter 6 nm) on α-Al_2O_3(0001) under a gas flow of 5 ml/min at 500 K: (a) Reciprocal space map around the Pd(111) Bragg reflection. The red line indicates the direction of the radial intensity profile; (b) The intensity of the Pd(111) Bragg reflection and evolution of mass 98 associated with MCH as a function of time; (c) Selected intensity profiles of the Pd(111) Bragg reflection. (d) The fraction of pure Pd (blue) and Pd_xC (green) phases (top panel) and the position of the Pd_xC diffraction peak as a function of time. The grey boxes indicate the exposure to MCH.

At the onset of the MCH flow, the Pd(111) Bragg peak shifts to lower diffraction angles. Then, the position of the peak remains constant under steady MCH partial pressure (Figure 1b). Subsequently, the feed was switched back to pure Ar, leading to a decrease of the MCH partial pressure. We observe that after a certain delay, the original position of the Pd(111) Bragg reflection is recovered. During the second MCH pulse, a similar behavior was observed. These observations suggest that structural changes in the supported Pd nanoparticles upon exposure of the catalyst to the reactant feed are highly reversible.

In order to obtain more detailed insights into the structure and phase composition of the Pd nanoparticles, we analyzed the intensity profile of the Pd(111) Bragg reflection. Selected profiles are shown in Figure 1c. Here, the profile obtained under Ar flow after the cleaning procedure is shown as the top trace. We resolved two peaks at diffraction angles of 4.056° and 3.940° yielding the lattice parameters of 0.389 nm and of 0.401 nm which are associated with the pure palladium and palladium carbide (Pd_xC) phases, respectively.[36] Note that the formation of the β-hydride phase in supported Pd nanoparticles is suppressed at 500 K.[24] The lattice parameter of the Pd_xC phase corresponds to an expansion of the Pd lattice by 3.1%. For the

fitting procedure, the position of the peak associated with the pure Pd phase was fixed. The component associated with the Pd_xC phase was allowed to vary between the values for pure Pd and Pd_6C. Pd_6C is the palladium carbide phase with the highest carbon content (14% C) reported in the literature.[29, 51]

The evolution of the contributions of pure Pd and the Pd_xC phases is plotted in Figure 1d as a function of time. The periods of time when the catalyst was exposed to MCH pulses are displayed as gray blocks. The fractions of pure Pd and Pd_xC phases were obtained by fitting intensity profiles obtained with an acquisition time of 1 s. In order to improve the signal-to-noise ratio, we also averaged over 15 consecutive intensity profiles. The corresponding data are plotted in Figure 1d in darker colors.

The ball models in Figure 1 depict the phase composition of the small Pd nanoparticles in the experimental regions (i)-(iii). Thus, after the cleaning procedure the small Pd nanoparticles consist of predominantly of pure Pd with a minor amount of Pd_xC. This phase composition remains stable under Ar flow (Figure 1, ball model (i)). As soon as MCH is added to the stream, the fraction of Pd_xC increases at the expense of the pure Pd phase. Eventually the majority of the material is transformed into the Pd_xC phase. This process is accompanied by a shift of the Pd_xC contribution to lower diffraction angles. The diffraction angle and the corresponding lattice parameter of the Pd_xC phase are plotted in Figure 1d (bottom panel) as a function of time. We note that the Pd_xC contribution shifts from a diffraction angle of 3.940° to 3.935°. The change in diffraction angle reflects an increasing carbon concentration, eventually approaching the value characteristic for the Pd_6C phase. We assume that the Pd_6C phase is covered by carbon deposits (Figure 1, ball model (ii)). The formation of carbon deposits during dehydrogenation of LOHCs over Pd(111) and supported Pd nanoparticles above 450 K was observed earlier by means of high-resolution synchrotron radiation photoelectron spectroscopy studies.[11, 14-15] The Pd_6C phase remains stable under MCH exposure. A similar behavior was previously reported in the literature.[26-27, 37, 51-52]

Subsequent exposure to pure Ar flow resulted in the decomposition of the Pd_6C yielding the pure Pd phase. The decrease of the Pd_6C signal is relatively slow at first and then rapidly accelerates indicating the transformation of the Pd_6C into the Pd_xC phase with lower carbon content. Note that the position of the Pd_xC peak correlates linearly with the carbon content in the Pd_xC phase.[53] The phase transition is marked by the shift of the corresponding Pd_xC peak to higher diffraction angles which indicates a decrease of carbon content in Pd_xC (see Figure 1d, bottom panel, 2000 s). Finally, the initial phase composition of the Pd nanoparticles is restored.

Note that at early stages of Pd_6C decomposition, we did not observe the formation of any new Pd_xC phase. This observation suggests that carbon is removed out of the Pd nanoparticle by segregating to the surface. We believe that under reaction conditions, there is facile diffusion of carbon in both directions, i.e. into and out of the Pd nanoparticles. The stability of the Pd_6C phase therefore depends on the rate of carbon formation and the rate of carbon removal by its reaction with hydrogen released into the gas phase during dehydrogenation of MCH. In the absence of a carbon and hydrogen source from the gas phase, carbon segregates to the surface resulting in decomposition of the Pd_6C phase which most likely contributes to the formation of carbon deposits. Typically, carbon deposits on Pd nanoparticles are found in the forms of carbon islands, carbon chains and filaments[31] (Figure 1, ball model (iii)). It was reported that the carbon filaments are precursor to graphene.[31] However, considering the high reproducibility of the phase composition of Pd nanoparticles under exposure to the second MCH pulse, we assume that the formation of graphene is not favorable under the applied experimental conditions.

3.2. MCH dehydrogenation over small Pd nanoparticles (6 nm) at high gas flow rate

In the next step, we investigated the behavior of the same sample, i.e. small Pd nanoparticles (6 nm) on α-Al_2O_3(0001), at a high gas flow rate of 100 ml/min. The same sample was used as in the experiment described in Section 3.1 after applying an in-situ cleaning procedure (see Section 2). We note that the analysis of the FWHM of the Pd(111) Bragg reflection revealed no change in the Pd particle size after cleaning. The absence of new features in the 2D reciprocal map (Figure 2a) suggests full recovery of the catalyst after cleaning.

Generally, the conversion of MCH decreases with increasing flow rate. As a result, the concentration of hydrogen in the gas phase over the catalyst surface will also decrease. This means that less surface carbon will be removed by the reaction with hydrogen. In other words, carbon formation will be accelerated under high gas flow conditions. As a result, the nucleation of graphene may occur more easily due to a higher amount of carbon at the surface.

Upon exposure to MCH we observe that the Pd(111) Bragg reflection shifts to lower diffraction angles (Figure 2b). This behavior is very similar to that observed under exposure to MCH at a low gas flow rate. Remarkably, under longer exposure to MCH, the reflection shifts slowly back to higher diffraction angles. Upon subsequent exposure to pure Ar, the diffraction angle remains practically unchanged (Figure 2b).

Similar as in section 3.1, the intensity profiles of the Pd(111) Bragg reflection were fitted with two contributions associated with the pure Pd and Pd_xC (Figure 2c). The evolution of the fractions of the two components is plotted in Figure 2d as a function of time. The initial composition of the Pd nanoparticles is represented by a dominant contribution from the pure Pd phase and minor contribution from Pd_xC (Figure 2, ball model (i)). This phase composition is stable under Ar. Upon switching to MCH, we observe a rapid increase of the Pd_xC contribution accompanied by its shift to lower diffraction angles. This observation indicates fast transformation into Pd_6C (Figure 2, ball model (ii)). Noteworthy, the Pd_6C is stable only for a short time at the high gas flow rate. As soon as the fraction of the Pd_6C phase reaches maximum, the Pd_6C phase starts to decompose yielding pure Pd covered by carbon deposits and graphene clusters (Figure 2, ball model (iii)). The fraction of the pure Pd phase gradually increases until the initial phase composition of clean Pd nanoparticles is nearly recovered

(Figure 2, ball model (iv)). The corresponding trend suggests that initial phase composition of Pd nanoparticles followed by complete extraction of subsurface carbon will be achieved after longer times under Ar flow.

The evolutions of the fractions of the Pd_xC phases under low and high flow rates of MCH are plotted on the same time scale in Supporting Information (Figure S3). We propose that the differences in stability of the Pd_6C phase at low and high flow rates of MCH result from the interplay between thermodynamic and kinetic effects during carbon deposition. We assume that under the conditions of low flow rate, the carbon deposition rate is lower due to partial removal of carbon by reaction with hydrogen from the gas phase and therefore is not sufficient for the nucleation of graphene. The situation changes at the high flow rate, where nucleation of graphene occurs approximately 120 seconds after starting the exposure to MCH. This observation is consistent with accelerated carbon formation due to lesser removal of carbon by reaction with hydrogen under high flow. Following the nucleation of graphene, the Pd_6C phase slowly decomposes due to segregation of carbon to the surface and its subsequent attachment to the growing graphene domains.[39] It was reported that part of the segregated carbon accumulates at the graphene/Pd interface and also leads to growth of multilayer graphene.[54] Our observation clearly shows that the Pd_6C phase can be formed, but it is metastable under a high flow rate of MCH.

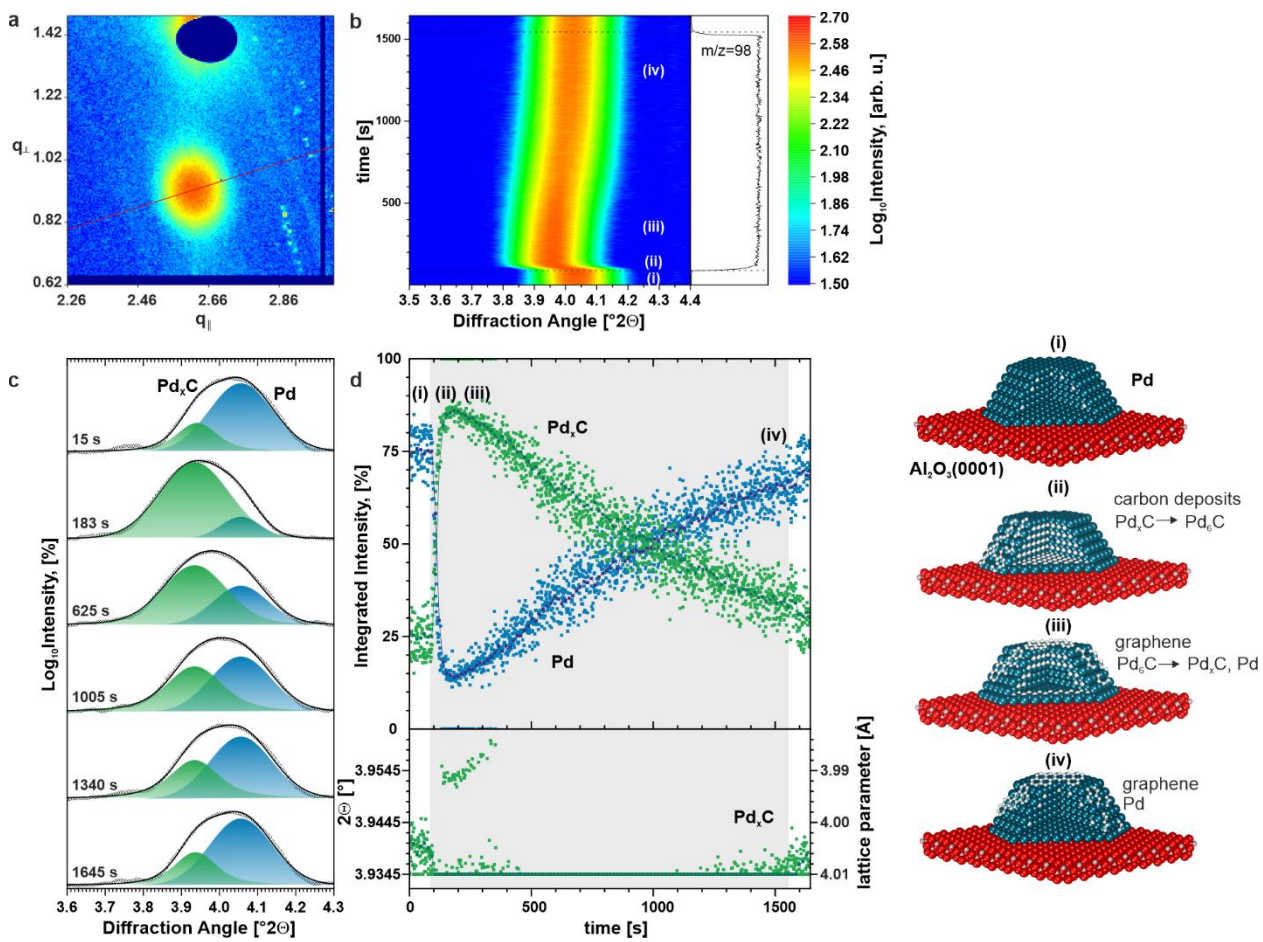

Figure 2. Small Pd nanoparticles (diameter 6 nm) on α-Al_2O_3(0001) under a gas flow of 100 ml/min at 500 K: (a) Reciprocal space map around the Pd(111) Bragg reflection. The red line indicates the direction of the radial intensity profile; (b) The intensity of the Pd(111) Bragg reflection and evolution of mass 98 associated with MCH as a function of time; (c) Selected intensity profiles of the Pd(111) Bragg reflection. (d) The fraction of pure Pd (blue) and Pd_xC (green) phases as a function of time and MCH partial pressure. The grey box indicates exposure to MCH.

3.3. MCH dehydrogenation over big Pd nanoparticles (15 nm) at low gas flow rate

Next, we investigated the influence of the particle size on the phase composition of the supported Pd nanoparticles. Considering a relatively large critical size of a graphene nucleus (about 5 nm as predicted on Pd(100)),[29] we expect that nucleation of graphene could be easier on the big Pd nanoparticles. In Figure 3, the corresponding data are displayed for big Pd nanoparticles (15 nm Pd nanoparticles on α-Al_2O_3(0001)). As for the experiments in sections 3.1 and 3.2, we show a 2D reciprocal space map around the Pd(111) Bragg reflection at 500 K (low Ar flow, 5 ml/min) (Figure 3a). In addition to the sharp Pd(111) reflection from epitaxial Pd nanoparticles, we observed a Debye-Scherrer ring arising from randomly oriented (non-epitaxial) Pd nanoparticles. Similar as in sections 3.1 and 3.2, we performed an analysis of the intensity profile along the radial direction indicated by the red line in Figure 3a. In this way, we selectively analyzed the

structure of Pd nanoparticles with a (111) epitaxy with respect to the Al_2O_3(0001) surface. This allowed us to compare the structural changes in the epitaxial Pd nanoparticles as a function of size. The structural changes in non-epitaxial Pd nanoparticles derived from the intensity profile of the Debye-Scherrer ring in comparison to epitaxial Pd nanoparticles are discussed in the Supporting Information. Note that a crystal truncation rod (CTR) from the Al_2O_3(0001) support (Figure 3a, white arrow) overlaps with the Bragg reflection from the Pd nanoparticles due to epitaxial in-plane orientation of Pd nanoparticles.[55-56] We note that due to slightly different rotational angle, the CTR is not visible in the case of small Pd nanoparticles (Figures 1a, 2a).

The intensity profile of the Pd(111) Bragg reflection is plotted in Figure 3b as a function of time and diffraction angle 2Θ. Additionally, we compare the evolution of the fractions of Pd_xC and Pd_6C (and their sum, Pd_6C + Pd_xC) for big (15 nm) and small (6 nm) Pd nanoparticles in Supporting Information (Figure S3). The differences are related to higher stability of the Pd_xC phases in the case of smaller Pd nanoparticles where the growth of graphene under the low flow rate of MCH is not favorable. In contrast to the small Pd nanoparticles, we observe a rapid shift of the Bragg reflection to higher diffraction angles at the onset of the MCH flow (at t = 200 s, Figure 3d). Then, the reflection gradually shifts to lower diffraction angles. The same shift is observed in the Debye-Scherrer ring (see Supporting Information for more detail). After a period of approximately 500 s in MCH, the Bragg reflection broadens and the maximum gradually shifts back to higher diffraction angles.

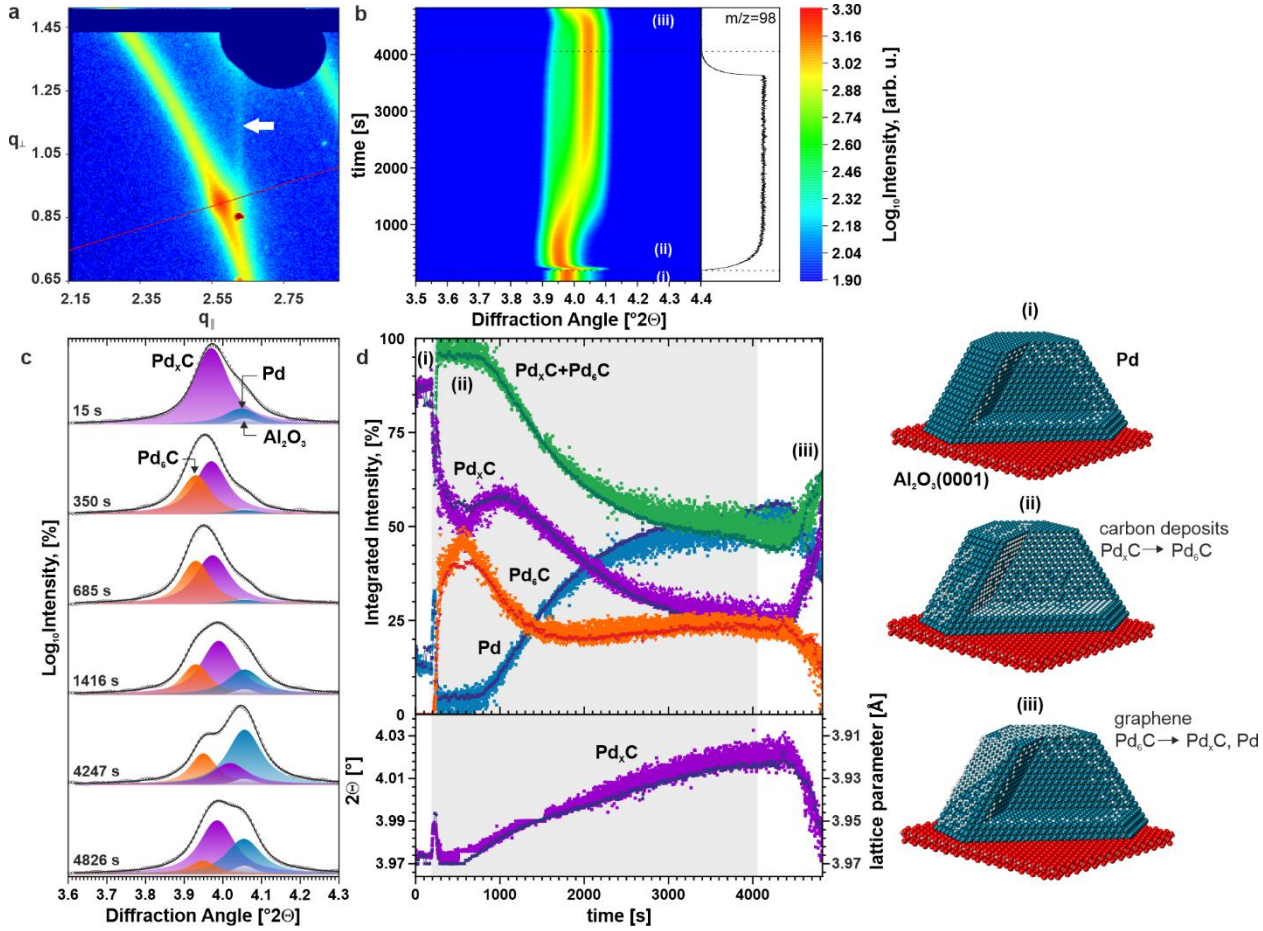

Figure 3. Big Pd nanoparticles (diameter 15 nm) on α-Al_2O_3(0001) under a flow of 5 ml/min at 500 K: (a) Reciprocal space map around the Pd(111) Bragg reflection. The red line indicates the direction of the radial intensity profile; The white arrow indicates the truncation rod from the α-Al_2O_3(0001) substrate; (b) The intensity of the Pd(111) Bragg reflection and evolution of mass 98 associated with MCH as a function of time; (c) Selected intensity profiles of the Pd(111) Bragg reflection; (d) Fractions of pure Pd (blue squares), Pd_6C (orange triangles), Pd_xC (purple triangles) phases, and the sum of the Pd_6C and Pd_xC contributions (green squares) as a function of time. The grey box indicates exposure to MCH.

Selected intensity profiles of the Bragg reflection are shown in Figure 3c. Here, the intensity profile obtained under Ar flow following the cleaning procedure is shown as the top trace. We resolved two peaks associated with the pure Pd and Pd_xC phases, respectively. The corresponding phase composition of Pd nanoparticles is schematically represented in Figure 3 (ball model (i)). The lattice parameter of the Pd_xC phase is 0.397 nm which corresponds to an expansion of the Pd lattice by 2.1%. Additionally, the contribution from the Al_2O_3 truncation rod was added to the fitting envelope (Figure 3c, top). The position of this contribution was fixed and its intensity was allowed to vary by ±20% during fitting.

We found that the rapid shift of the Bragg spot upon MCH exposure is caused by a shift of the Pd_xC contribution from a diffraction angle of 3.974° to 3.994° which corresponds to a change in the lattice parameter from 0.397 to 0.395 nm. This

observation suggests that a small amount of carbon rapidly segregated to the surface of the Pd nanoparticle. We suggest that upon MCH exposure, carbon is removed from the Pd nanoparticle by reaction with hydrogen formed upon dehydrogenation of MCH. This process becomes less efficient upon progressive carbon deposition under a continuous flow of MCH. Inward diffusion of carbon into the nanoparticles becomes dominant and the Pd_xC contribution shifts back to lower diffraction angle.

Notably, a new distinct component emerges at a diffraction angle of 3.930°. This feature can be assigned to the Pd_6C phase. In contrast, the Pd_xC phase in the Debye-Scherrer ring gradually transforms into the Pd_6C phase without the emergence of any new peak (see Supporting Information, sections S4 and S5). The corresponding 2D reciprocal space map shows the splitting of both the Debye-Scherrer ring and the Bragg spot (Figure S6). Growth of the Pd_6C phase is accompanied by a decrease of the signal from the pure Pd phase which eventually vanishes completely (Figure 3c, 350 s). In the meantime, the two carbide phases, Pd_6C and Pd_xC, coexist. The corresponding phase composition is shown in Figure 3 (ball model (ii)). This observation is in a strong contrast to the small nanoparticles where only one type of carbide was detected at a given time.

In Figure 3d, we show the evolution of fractions of Pd, Pd_6C and Pd_xC (and the combined contributions from Pd_6C and Pd_xC). The broadening of the Bragg reflection (Figure 3b, at $t > 490$ s) under constant flow of MCH is caused by the reappearance of the pure Pd phase while the Pd_6C phase is still present. The Pd component grows first at the expense of Pd_6C and later at the expense of Pd_xC (Figure 3d). Decomposition of Pd_xC is accompanied by a gradual shift of the corresponding contribution to higher diffraction angles (see Figure 3d, lower panel). Overall, the total contribution from the Pd_6C and Pd_xC phases remains constant for about 500 seconds (Figure 3d) and decreases thereafter. We propose that this delay is caused by the nucleation of graphene. Once the graphene nucleus is formed, the carbide phases start to decompose due to segregation of carbon to the surface and subsequent attachment to the graphene deposits.[39] It is noteworthy that the fraction of the Pd_6C phase stops to decrease further at around 1700 s. At this point only the Pd_xC phase is consumed and leads to further growth of the Pd phase (Figure 3d). The reason for this behavior is not clear. A possible explanation may involve the coexistence of differently shaped or sized nanoparticles on which the nucleation of the graphene phase is suppressed and, as a result, no carbon is extracted after the formation of Pd_6C. After switching back to a flow of pure Ar, the phase composition of the supported Pd nanoparticles remains practically unchanged for approximately 400 s. Then, the residual Pd_6C starts to decompose yielding pure Pd and Pd_xC covered by carbon deposits and graphene (Figure 3d, model (iii)).

The size distribution of Pd nanoparticles after the exposure to MCH and Ar at 500 K was analyzed by SEM (see Supporting Information, Figure S2). Briefly, we found significant broadening of the size distribution resulting in the average diameter of Pd nanoparticles of 19.2±8.0 nm. The corresponding density of Pd nanoparticles decreased to 3.4×10^{14} m^{-2}. This observation suggests sintering of Pd nanoparticles under operation conditions.

Conclusions

We have investigated the dynamic formation and decomposition of Pd carbides in a Pd/α-Al_2O_3(0001) model catalyst by in-situ HE-GIXRD during dehydrogenation of a model liquid organic hydrogen carrier. The most important observations are listed below and are illustrated in Figure 4:

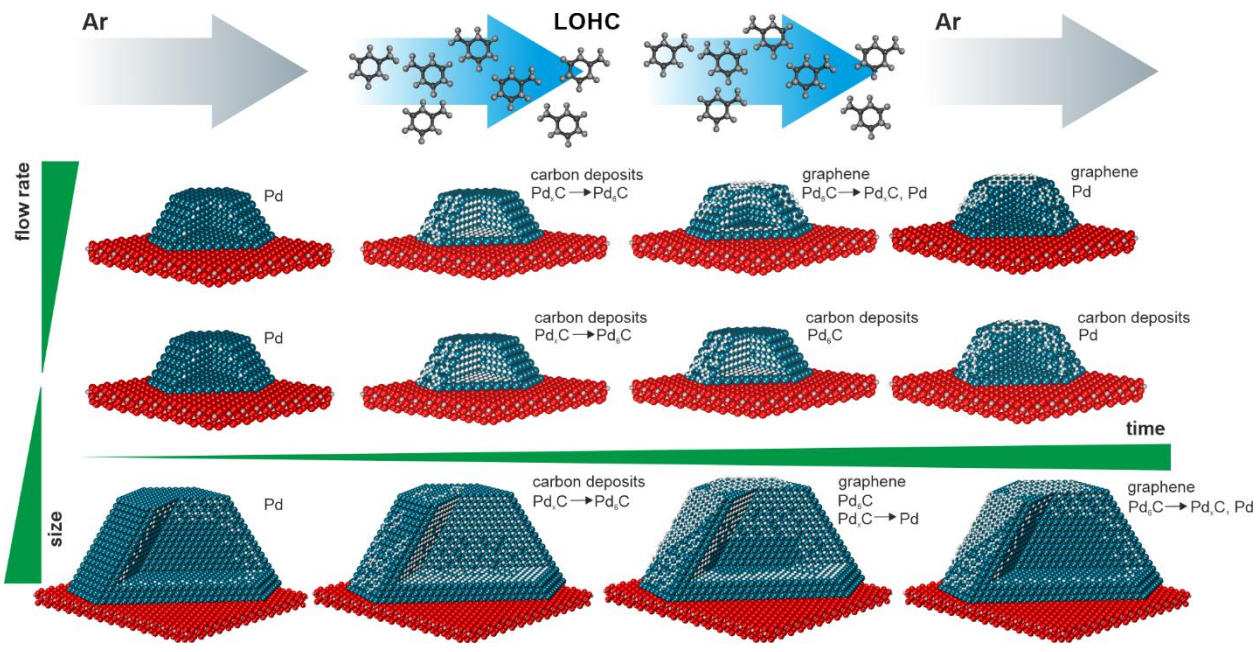

Figure 4. Schematic representation of the structural changes in the model $Pd/Al_2O_3(0001)$ catalysts as a function of the flow rate of the reactant, size of supported Pd nanoparticles, and time of the catalyst on stream at 500 K.

1) Exposure of small Pd nanoparticles (6 nm) to MCH at 500 K triggers the formation of a palladium carbide phase (Pd_xC). The carbon content in the Pd_xC phase gradually increases yielding the Pd_6C phase. The stability of the Pd_6C critically depends on the composition of the reactant feed. At low MCH flow (i.e. high H_2 partial pressure), the Pd_6C phase is stable but decomposes in pure Ar. The stability of the Pd_6C results from the balance between carbon formation and carbon consumption (mainly by reaction with hydrogen released upon the dehydrogenation of LOHC) under the flow of MCH. In the absence of the carbon source from the gas phase, Pd_6C decomposes due to carbon segregation to the surface of Pd nanoparticles. This behavior is fully reproducible upon repeated exposure to MCH under similar conditions. At a high flow rate of MCH (i.e. low H_2 partial pressure), the Pd_6C phase is formed but then rapidly decomposes. Decomposition of the Pd_6C is triggered by the nucleation and growth of graphene deposits on the surface of Pd nanoparticles.

2) On larger Pd nanoparticles (diameter 15 nm) a different behavior is observed. Upon exposure to MCH, we observe the coexistence of two Pd carbide phases, i.e. Pd_6C and Pd_xC. With increasing time on stream, the Pd_xC phase is converted to Pd_6C. Upon extended exposure to MCH, we observe decomposition of the Pd_6C and Pd_xC phases and the pure Pd phase is recovered. We propose that decomposition of the carbide occurs as a result of the formation of carbon deposits in the form of graphene. Because of slow nucleation, the graphene deposits are formed after an induction period.

Our results show that Pd catalysts may adopt very different states under conditions of LOHC dehydrogenation: The Pd nanoparticles may be present in the form of carbides with varying carbon content from Pd_xC up to Pd_6C and in the form of pure Pd nanoparticles covered with graphene deposits. Formation and decomposition of these phases results from a complex interplay between their thermodynamic stability and the kinetics of carbon formation and consumption. The formation kinetics of the carbide phases strongly depends on the particle size. LOHC dehydrogenation is performed under dynamic operation conditions and the activation and deactivation phenomena which are typically observed in these processes are most likely related to dynamic formation of carbide phases.

Conflicts of interest

There are no conflicts to declare.

Acknowledgements

The authors acknowledge financial support from the Free State of Bavaria through its institutional and project-based support for the Helmholtz-Institute Erlangen-Nürnberg for Renewable Energies. The authors acknowledge additional financial support from the Federal Ministry of Education and Research (project 05K19WE1). The authors acknowledge financial support by the Deutsche Forschungsgemeinschaft (DFG) including the Cluster of Excellence "Engineering of Advanced Materials" (project EXC 315). Parts of this research were carried out at the DESY NanoLab, DESY, a member of the Helmholtz Association (HGF). Partial financial support by the DESY strategy fund (DSF) is acknowledged. We acknowledge the European Synchrotron Radiation Facility for provision of synchrotron radiation facilities and financial support. We thank Jan-Christian Schober for help in sample preparation and XRR analysis and Arno Jeromin for SEM analysis.

Notes and references

1 D. Teichmann, W. Arlt, P. Wasserscheid and R. Freymann, *Energy Environ. Sci.*, 2011, **4**, 2767-2773.
2 M. Niermann, S. Drünert, M. Kaltschmitt and K. Bonhoff, *Energy Environ. Sci.*, 2019, **12**, 290-307.
3 P. Preuster, A. Alekseev and P. Wasserscheid, *Annu. Rev. Chem. Biomol. Eng.*, 2017, **8**, 445-471.
4 L. Li, M. Yang, Y. Dong, P. Mei and H. Cheng, *Int. J. Hydrogen Energy*, 2016, **41**, 16129-16134.
5 P. Preuster, C. Papp and P. Wasserscheid, *Acc. Chem. Res.*, 2017, **50**, 74-85.
6 M. Schwarz, P. Bachmann, T. N. Silva, S. Mohr, M. Scheuermeyer, F. Späth, U. Bauer, F. Düll, J. Steinhauer, C. Hohner, T. Döpper, H. Noei, A. Stierle, C. Papp, H.-P. Steinrück, P. Wasserscheid, A. Görling and J. Libuda, *Chem. - Eur. J.*, 2017, **23**, 14806–14818.
7 P. C. Rao and M. Yoon, *Energies*, 2020, **13**, 6040.
8 A. Bulgarin, H. Jorschick, P. Preuster, A. Bösmann and P. Wasserscheid, *Int. J. Hydrogen Energy*, 2020, **45**, 712-720.
9 P. M. Modisha, C. N. M. Ouma, R. Garidzirai, P. Wasserscheid and D. Bessarabov, *Energy & Fuels*, 2019, **33**, 2778-2796.
10 L. Zhou, L. Sun, L. Xu, C. Wan, Y. An and M. Ye, *Catalysts*, 2020, **10**, 648.
11 M. Amende, C. Gleichweit, T. Xu, O. Höfert, M. Koch, P. Wasserscheid, H. P. Steinrück, C. Papp and J. Libuda, *Catal. Lett.*, 2016, **146**, 851-860.
12 P. Bachmann, J. Steinhauer, F. Späth, F. Düll, U. Bauer, R. Eschenbacher, F. Hemauer, M. Scheuermeyer, A. Bösmann, M. Büttner, C. Neiß, A. Görling, P. Wasserscheid, H.-P. Steinrück and C. Papp, *J. Chem. Phys.*, 2019, **151**, 144711.
13 C. Gleichweit, M. Amende, O. Höfert, T. Xu, F. Späth, N. Brückner, P. Wasserscheid, J. Libuda, H.-P. Steinrück and C. Papp, *J. Phys. Chem. C*, 2015, **119**, 20299-20311.
14 M. Amende, S. Schernich, M. Sobota, I. Nikiforidis, W. Hieringer, D. Assenbaum, C. Gleichweit, H.-J. Drescher, C. Papp, H.-P. Steinrück, A. Görling, P. Wasserscheid, M. Laurin and J. Libuda, *Chem. - Eur. J.*, 2013, **19**, 10854-10865.
15 M. Sobota, I. Nikiforidis, M. Amende, B. Sanmartín Zanón, T. Staudt, O. Höfert, Y. Lykhach, C. Papp, W. Hieringer, M. Laurin, D. Assenbaum, P. Wasserscheid, H.-P. Steinrück, A. Görling and J. Libuda, *Chem. - Eur. J.*, 2011, **17**, 11542–11552.
16 C. Gleichweit, M. Amende, U. Bauer, S. Schernich, O. Höfert, M. P. A. Lorenz, W. Zhao, M. Müller, M. Koch, P. Bachmann, P. Wasserscheid, J. Libuda, H.-P. Steinrück and C. Papp, *J. Chem. Phys.*, 2014, **140**, 204711.
17 M. Amende, C. Gleichweit, S. Schernich, O. Höfert, M. P. A. Lorenz, W. Zhao, M. Koch, K. Obesser, C. Papp, P. Wasserscheid, H.-P. Steinrück and J. Libuda, *J. Phys. Chem. Lett.*, 2014, **5**, 1498-1504.

18 A. L. Bugaev, O. A. Usoltsev, A. Lazzarini, K. A. Lomachenko, A. A. Guda, R. Pellegrini, M. Carosso, J. G. Vitillo, E. Groppo, J. A. van Bokhoven, A. V. Soldatov and C. Lamberti, *Faraday Discuss.*, 2018, **208**, 187-205.
19 D. Teschner, J. Borsodi, A. Wootsch, Z. Révay, M. Hävecker, A. Knop-Gericke, S. D. Jackson and R. Schlögl, *Science*, 2008, **320**, 86.
20 D. Teschner, Z. Révay, J. Borsodi, M. Hävecker, A. Knop-Gericke, R. Schlögl, D. Milroy, S. D. Jackson, D. Torres and P. Sautet, *Angew. Chem., Int. Ed.*, 2008, **47**, 9274-9278.
21 K. M. Neyman and S. Schauermann, *Angew. Chem., Int. Ed.*, 2010, **49**, 4743-4746.
22 M. García-Mota, B. Bridier, J. Pérez-Ramírez and N. López, *J. Catal.*, 2010, **273**, 92-102.
23 M. W. Tew, M. Janousch, T. Huthwelker and J. A. van Bokhoven, *J. Catal.*, 2011, **283**, 45-54.
24 R. Schuster, F. Waidhas, M. Bertram, H. Runge, S. Geile, R. Shayduk, M. Abuín, V. Vonk, H. Noei, Y. Lykhach, F. Bertram, A. Stierle and J. Libuda, *Catal. Lett.*, 2018, **148**, 2901-2910.
25 M. Bowker, C. Morgan, N. Perkins, R. Holroyd, E. Fourre, F. Grillo and A. MacDowall, *J. Phys. Chem. B*, 2005, **109**, 2377-2386.
26 H. Gabasch, K. Hayek, B. Klötzer, A. Knop-Gericke and R. Schlögl, *J. Phys. Chem. B*, 2006, **110**, 4947-4952.
27 M. Morkel, V. V. Kaichev, G. Rupprechter, H. J. Freund, I. P. Prosvirin and V. I. Bukhtiyarov, *J. Phys. Chem. B*, 2004, **108**, 12955-12961.
28 L. Gracia, M. Calatayud, J. Andrés, C. Minot and M. Salmeron, *Phys. Rev. B*, 2005, **71**, 033407.
29 N. Seriani, F. Mittendorfer and G. Kresse, *J. Chem. Phys.*, 2010, **132**, 024711.
30 H. Grönbeck and C. Barth, *J. Phys. Chem. C*, 2019, **123**, 4360-4370.
31 C. Barth, *J. Phys. Chem. C*, 2018, **122**, 522-529.
32 O. Balmes, A. Resta, D. Wermeille, R. Felici, M. E. Messing, K. Deppert, Z. Liu, M. E. Grass, H. Bluhm, R. v. Rijn, J. W. M. Frenken, R. Westerström, S. Blomberg, J. Gustafson, J. N. Andersen and E. Lundgren, *Phys. Chem. Chem. Phys.*, 2012, **14**, 4796-4801.
33 F. Viñes, C. Loschen, F. Illas and K. M. Neyman, *J. Catal.*, 2009, **266**, 59-63.
34 L. Nykänen, J. Andersin and K. Honkala, *Phys. Rev. B*, 2010, **81**, 075417.
35 S. M. Kozlov, I. V. Yudanov, H. A. Aleksandrov and N. Rösch, *Phys. Chem. Chem. Phys.*, 2009, **11**, 10955-10963.
36 S. B. Ziemecki, G. A. Jones, D. G. Swartzfager, R. L. Harlow and J. Faber, *J. Am. Chem. Soc.*, 1985, **107**, 4547-4548.
37 J. A. McCaulley, *J. Phys. Chem.*, 1993, **97**, 10372-10379.
38 J. A. McCaulley, *Phys. Rev. B*, 1993, **47**, 4873-4879.
39 H. S. Mok, A. Ebnonnasir, Y. Murata, S. Nie, K. F. McCarty, C. V. Ciobanu and S. Kodambaka, *Appl. Phys. Lett.*, 2014, **104**, 101606.
40 A. Stierle, J. Gustafson and E. Lundgren, in *Operando Research in Heterogeneous Catalysis*, eds. J. Frenken and I. Groot, Springer International Publishing, Cham2017, pp. 59-87.
41 J. Gustafson, M. Shipilin, C. Zhang, A. Stierle, U. Hejral, U. Ruett, O. Gutowski, P. A. Carlsson, M. Skoglundh and E. Lundgren, *Science*, 2014, **343**, 758-761.
42 U. Hejral, P. Müller, O. Balmes, D. Pontoni and A. Stierle, *Nat. Commun.*, 2016, **7**, 10964.
43 U. Hejral, P. Müller, M. Shipilin, J. Gustafson, D. Franz, R. Shayduk, U. Rütt, C. Zhang, L. R. Merte, E. Lundgren, V. Vonk and A. Stierle, *Phys. Rev. B*, 2017, **96**, 195433.
44 P. Nolte, A. Stierle, N. Kasper, N. Y. Jin-Phillipp, H. Reichert, A. Rühm, J. Okasinski, H. Dosch and S. Schöder, *Phys. Rev. B*, 2008, **77**, 115444.
45 M. Shipilin, U. Hejral, E. Lundgren, L. R. Merte, C. Zhang, A. Stierle, U. Ruett, O. Gutowski, M. Skoglundh, P.-A. Carlsson and J. Gustafson, *Surf. Sci.*, 2014, **630**, 229-235.
46 M. Shipilin, A. Stierle, L. R. Merte, J. Gustafson, U. Hejral, N. M. Martin, C. Zhang, D. Franz, V. Kilic and E. Lundgren, *Surf. Sci.*, 2017, **660**, 1-8.
47 P. Müller, U. Hejral, U. Rütt and A. Stierle, *Phys. Chem. Chem. Phys.*, 2014, **16**, 13866-13874.
48 R. van Rijn, M. D. Ackermann, O. Balmes, T. Dufrane, A. Geluk, H. Gonzalez, H. Isern, E. de Kuyper, L. Petit, V. A. Sole, D. Wermeille, R. Felici and J. W. M. Frenken, *Rev. Sci. Instrum.*, 2010, **81**, 014101.
49 A. Stierle, T. F. Keller, H. Noei, V. Vonk and R. Roehlsberger, *Journal of large-scale research facilities*, 2016, **2**, 1-9.
50 P. Scherrer, in *Kolloidchemie Ein Lehrbuch*, ed. R. Zsigmondy, Springer Berlin Heidelberg, Berlin, Heidelberg, 1912, pp. 387-409.
51 S. B. Ziemecki, G. A. Jones and D. G. Swartzfager, *J. Less-Common Met.*, 1987, **131**, 157-162.
52 M. W. Tew, M. Nachtegaal, M. Janousch, T. Huthwelker and J. A. van Bokhoven, *Phys. Chem. Chem. Phys.*, 2012, **14**, 5761-5768.
53 R. H. Siller, R. B. McLellan and M. L. Rudee, *J. Less-Common Met.*, 1969, **18**, 432-433.
54 Y. Murata, S. Nie, A. Ebnonnasir, E. Starodub, B. B. Kappes, K. F. McCarty, C. V. Ciobanu and S. Kodambaka, *Phys. Rev. B*, 2012, **85**, 205443.
55 K. Mašek and V. Matolín, *Eur. Phys. J. D*, 1999, **9**, 557-560.
56 A. Aleman, C. Li, H. Zaid, H. Kindlund, J. Fankhauser, S. V. Prikhodko, M. S. Goorsky and S. Kodambaka, *J Vac Sci Technol A*, 2018, **36**, 030602-030602.